



THE UNIVERSITY *of* EDINBURGH

Edinburgh Research Explorer

Hydrodynamic analysis of a ducted, open centre tidal stream turbine using blade element momentum theory

Citation for published version:

Allsop, S, Peyrard, C, Thies, PR, Boulougouris, E & Harrison, G 2017, 'Hydrodynamic analysis of a ducted, open centre tidal stream turbine using blade element momentum theory' *Ocean Engineering*, vol. 141, pp. 531-542. DOI: 10.1016/j.oceaneng.2017.06.040

Digital Object Identifier (DOI):

[10.1016/j.oceaneng.2017.06.040](https://doi.org/10.1016/j.oceaneng.2017.06.040)

Link:

[Link to publication record in Edinburgh Research Explorer](#)

Document Version:

Peer reviewed version

Published In:

Ocean Engineering

General rights

Copyright for the publications made accessible via the Edinburgh Research Explorer is retained by the author(s) and / or other copyright owners and it is a condition of accessing these publications that users recognise and abide by the legal requirements associated with these rights.

Take down policy

The University of Edinburgh has made every reasonable effort to ensure that Edinburgh Research Explorer content complies with UK legislation. If you believe that the public display of this file breaches copyright please contact openaccess@ed.ac.uk providing details, and we will remove access to the work immediately and investigate your claim.



Hydrodynamic analysis of a ducted, open centre tidal stream turbine using blade element momentum theory

Steven Allsop ^{A, B, C, *}, Christophe Peyrard ^{B, C}, Philipp R. Thies ^D, Evangelos Boulougouris ^E, Gareth P. Harrison ^F

^A Industrial Doctoral Centre for Offshore Renewable Energy (IDCORE), University of Edinburgh, EH93LJ, UK

^B EDF R&D – Electricité de France Research and Development (EDF R&D), LNHE, 6 Quai Watier, 78400 Chatou, France

^C Saint-Venant Hydraulics Laboratory, Université Paris-Est, 6 quai Watier, 78400 Chatou, France

^D College of Engineering, Mathematics and Physical Sciences, Renewable Energy Group, University of Exeter, TR109FE, UK

^E Department of Naval Architecture, Ocean and Marine Engineering, University of Strathclyde, Glasgow G40LZ, UK

^F Institute for Energy Systems, School of Engineering, University of Edinburgh, King's Buildings, Edinburgh, EH93JL, UK

* steven-externe.allsop@edf.fr

Abstract

This paper analyses two different configurations of horizontal axis Tidal Stream Turbines (TSTs) using a Blade Element Momentum Theory (BEMT) model. Initially, a 'conventional' three bladed and bare turbine is assessed, comparing against experimental measurements and existing literature. Excellent agreement is seen, increasing confidence in both the implementation of the theory and the applicability of the method. The focus of the paper lies on the analysis of a ducted and open centre

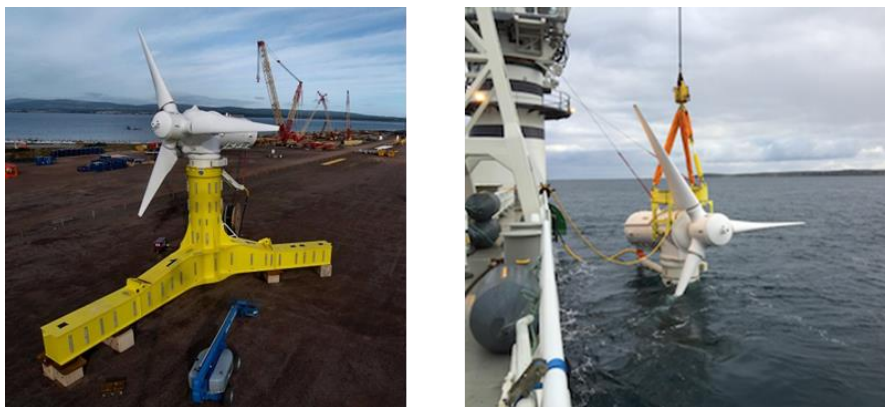
turbine. An analytical adjustment to the BEMT model is applied, using empirical expressions detailed in the literature which are devised from Computational Fluid Dynamics (CFD) studies. This is modified to a symmetrical duct profile, calibrating certain geometrical parameters against blade resolved CFD studies of a bi-directional device. The results are validated with a coupled CFD blade element model (RANS BEM), where both models align very closely (within 2%) for most tip speed ratios (TSRs), including the peak power condition. Over predictions are seen at higher TSRs of up to 25% in power and 13% in thrust at TSR=5, due to model limitations in replicating fully the complex flow interactions around the hub and the open centre. The presented approach benefits from significantly lower computational requirements, several orders of magnitude lower than reported in the RANS-BEM case, allowing practicable engineering assessments of turbine performance and reliability.

Keywords: Tidal stream turbine, marine current turbine, ducted, bidirectional, open centre, blade element momentum

1 Introduction

2 Tidal Stream Turbine (TST) technology has been in the early stage developmental phase for a
3 number of years, as engineering challenges in designing for extreme operating environments,
4 combined with political and environmental factors has limited the rate of maturity. One of the
5 earliest landmark projects was the MCT SeaGen, a 1.2MW twin rotor device installed in the
6 Strangford Loch, Northern Ireland in 2008, due to be decommissioned this year after generating
7 10GWh electricity (ReNews 2016). Despite hindrances in the industry, recent progression has led to
8 the deployment of full scale arrays around the UK and France. Although there are many designs of
9 tidal energy converters, the industry appears to have converged upon two configurations, which
10 have seen the furthest advancement to date in terms of commercial scale deployment.

11 The first is a 'classical', 3 bladed horizontal axis design, similar to its wind turbine counterpart. The
12 MeyGen project phase 1A (MeyGen 2016) has seen the installation of its first three turbines of a
13 6MW array as of January 2017 in the Pentland Firth, Scotland (shown in Figure 1-1).



14
15 *Figure 1-1 Andritz Hydro Hammerfest 1.5MW rated TST (left, image credit: Atlantis) with installation into the Pentland*
16 *Firth, Scotland (right, image credit: MeyGen) as part of the MeyGen Phase 1A deployment*

17 The second is a high solidity, ducted and open-centre turbine design. Ducts are primarily designed to
18 increase the power extraction by increasing the mass flow rate through the rotor. Additional
19 benefits include aligning yawed flow, providing a housing for a direct drive rim generator and
20 removing the requirement for mechanical systems such as a gearbox. DCNS / OpenHydro have

21 installed a pair of 500kW rated capacity turbines (shown in Figure 1-2), as a demonstration array in
22 Paimpol-Bréhat, Northern France, in collaboration with EDF.



23
24 *Figure 1-2 DCNS / OpenHydro 500 kW rated turbine (left, image credit: The Canadian Press) with installation at the Paimpol*
25 *Bréhat site, Northern France (right, image credit: DCNS)*

26 Hydrodynamic assessments are performed in order to gain insight into various aspects of the
27 turbine. An extensive range of numerical models exist, each designed to perform different tasks and
28 selected depending on the area of interest or objective of the study. Highly complex, high fidelity
29 models are commonly used in design refinement, or to perform detailed assessments of turbine
30 components under specific operating conditions. These can also be used to determine wake
31 formation to measure the impact of the turbines on the tidal flow, as well as to describe the
32 interactions of multiple turbines in an array.

33 Simpler models employ a more basic approach which are able to compute the force distributions
34 along the rotor blades, and determine the overall performance of a turbine, aiding early stage
35 decision making on optimal device designs for specific sites. Significantly lower computational
36 requirements and fast processing time can be exploited for engineering applications where many
37 analyses are required, such as performing numerous design iterations, analysing multiple or varying
38 inflow conditions, or assessing fatigue loading.

39 Several industrial and academic codes are based on BEMT, (Batten et al. 2007; Masters et al. 2011;
40 DNV GL Garrad Hassan 2012) among which is a commercial standard software tool, 'Tidal Bladed', by
41 the classification society DNV-GL. These models are simple, but are well established and reliable,

42 based on experience from the wind turbine industry. The BEMT code developed in this study is
43 initially applied to a bare, 3-bladed turbine, where a full validation study is detailed in (Allsop et al.
44 2016). However, the availability of such models for ducted, high solidity and open centre turbines is
45 limited. At present, these types of devices are analysed using blade resolved CFD, which has a high
46 computational requirement and is therefore not practical for multiple calculation applications. Less
47 computationally intensive alternatives have been applied (Fleming et al. 2011; Turnock et al. 2011;
48 Belloni et al. 2016) based on a coupled Reynolds Averaged Navier Stokes with blade element
49 momentum (RANS-BEM), where case studies report good comparison with fully blade resolved
50 studies, at a fraction of the processing time (McIntosh et al. 2012).

51 This paper aims to assess the performance of an analytical / empirical methodology to account for
52 the presence of a duct, which is implemented within a BEMT code. This ducted BEMT model is
53 applied to a bi-directional ducted turbine and results are compared with those of a coupled RANS
54 BEM simulation.

55 The remainder of this paper is structured into 5 main sections: i) a brief outline of the underlying
56 theory considered in the model; ii) the setup and implementation of the numerical model; iii) main
57 results for the three bladed and ducted, open centre turbine; iv) a discussion comparing the
58 different numerical models and implications as well as v) a conclusion of the main findings and
59 recommendations for further work.

60 2 Methodology

61 The principles of BEMT are well defined in the literature, where this section aims to give a brief
62 outline of the methodology. For further details and full derivations, the reader is referred to the
63 following texts (Burton et al. 2011; DNV GL Garrad Hassan 2012; Moriarty & Hansen 2005).

64 Section 2.1 describes the BEMT model for a classical 3 bladed, bare turbine, with Section 2.2
65 outlining the adaptations based on an analytical framework to account for the presence of a duct.

66 Section 2.3 defines output parameters that are used to validate the two models, with Sections 2.4
67 and 2.5 defining various correction factors in order to account for physical occurrences that are
68 neglected in the BEMT.

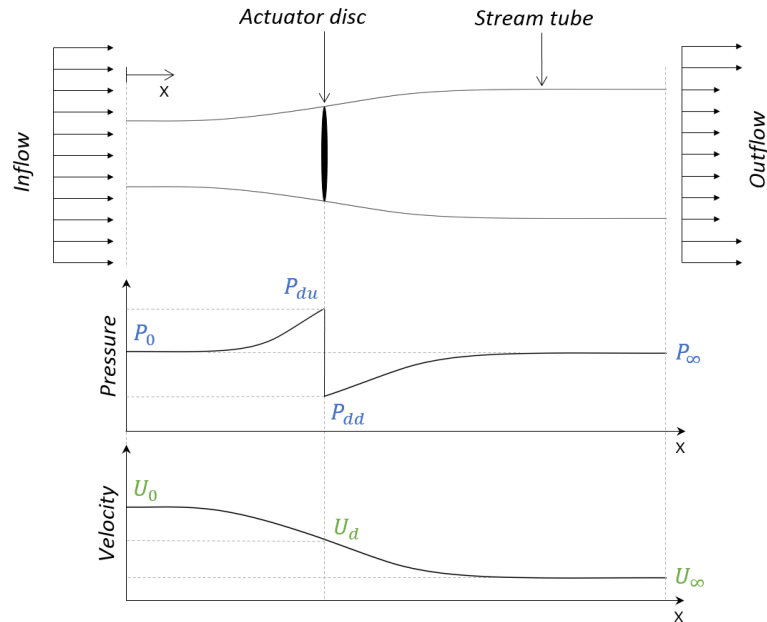
69 2.1 Blade element momentum theory

70 One-dimensional momentum theory models the turbine as an infinitely thin, semi-permeable
71 actuator disc exerting zero friction, bounded by a stream-tube (Figure 2-1). Flow velocities and
72 pressures at various locations along this control volume can be related using continuity and
73 Bernoulli's equations. The axial force (thrust) on the disc as a result of the change in pressure can be
74 equated to the change in axial momentum. The disc is split into a number of discrete annular rings as
75 shown in Figure 2-2a, assuming the momentum is extracted only from fluid passing through each
76 individual ring. The pressure / momentum balance can be applied independently to each ring such
77 that:

$$78 \quad dT = 4\pi\rho U_0^2 a(1-a)rdr$$

79 *eq. 1*

80 Where: $a = (U_0 - U_d) / U_0 = (U_0 - U_\infty) / 2U_0$ is the axial induction factor, dT is the element thrust
81 (N), ρ is the fluid density (kg m^{-3}), U_0 is the reference upstream velocity (m s^{-1}), U_d is the flow velocity
82 at the disc (m s^{-1}), r is the local element mean radius (m) and dr is the radial length of each ring (m).



83

84 *Figure 2-1 Schematic of the actuator disc model within a stream-tube, showing a representation of axial changes in*
 85 *pressure and velocity*

86 Associated with the change in axial momentum of the fluid as a result of the presence of the disc is
 87 also a change in angular momentum as a result of the turbine rotation. The fluid entering the turbine
 88 is considered straight, with zero rotational motion. The fluid passing through the rotating disc exerts
 89 a torque on the rotor, which requires an equal and opposite torque imposed on the fluid. This
 90 reaction torque causes the fluid to rotate in an opposite direction to turbine rotation. This has an
 91 associated gain in angular momentum, as the wake flow now has a velocity component tangential to
 92 the rotation (see Figure 2-2b). This increase in angular momentum can be related to the torque of
 93 each annular ring as a function of the tangential velocity and radial position:

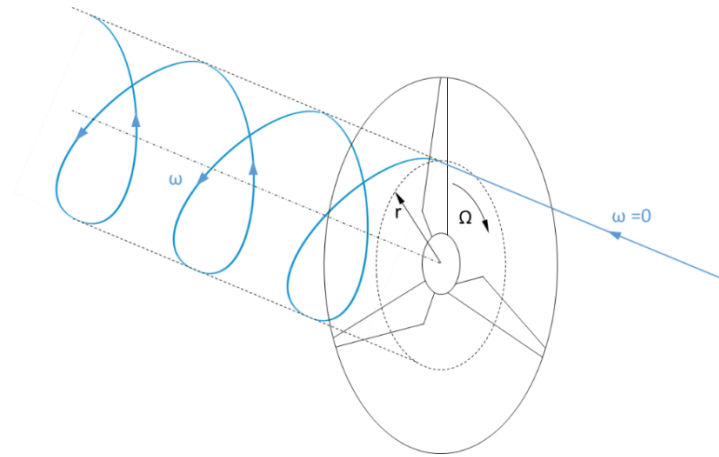
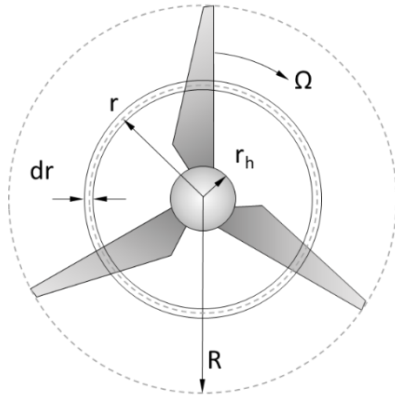
94

$$dQ = 4\pi\rho a' \Omega U_0 (1 - a) r^3 dr$$

95

eq. 2

96 Where: $a' = \omega / 2\Omega$ is the tangential induction factor which expresses the change in tangential
 97 velocity, dQ is the element torque (N m), ω the angular velocity of the wake (rad s^{-1}) and Ω the
 98 angular velocity of the turbine (rad s^{-1}).



99

100 *Figure 2-2 a) split of rotor disc into annular rings compared to overall turbine geometry (left) b) depiction of a particle*
 101 *interacting with rotor showing changes in rotational velocity (right)*

102 Blade element theory divides the blade into a number of discrete hydrofoil sections, which are
 103 analysed two dimensionally, neglecting any span-wise (radial) interactions. The flow at each 2D
 104 element has associated axial and tangential components of velocity, with the inflow angle (ϕ)
 105 located between (see Figure 2-3). The aerodynamic lift and drag forces on the blade element act
 106 parallel and perpendicular to this inflow angle, and can be determined using the standard aerofoil
 107 equations for lift and drag (DNV GL Garrad Hassan 2012):

$$dL = \frac{1}{2} C_L \rho W^2 c dr$$

eq. 3

$$dD = \frac{1}{2} C_D \rho W^2 c dr$$

eq. 4

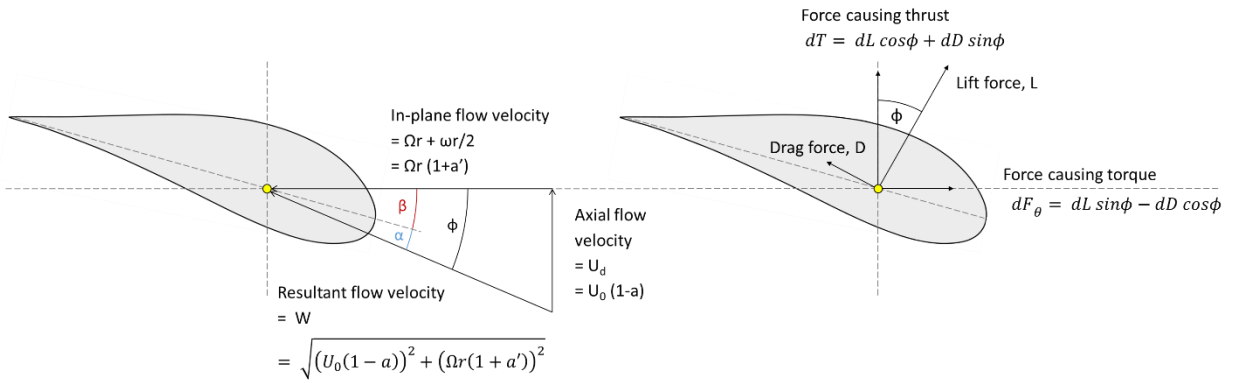
108 Where W is the resultant fluid velocity (m s^{-1}) and c the blade chord (m). Coefficients of lift (C_L) and
 109 drag (C_D) are input from two dimensional aerofoil data as a function of angle of attack (α), which can
 110 be determined from the inflow angle (ϕ) and the geometrical twist down the blade length (β). The
 111 forces causing thrust and torque can then be resolved trigonometrically, where B is the number of
 112 blades:

$$dT = \frac{1}{2} \rho W^2 B c (C_L \cos \phi + C_D \sin \phi) dr$$

eq. 5

$$dQ = \frac{1}{2} \rho W^2 B c (C_L \sin \phi - C_D \cos \phi) r dr$$

eq. 6



113

114 *Figure 2-3 a) Blade element flow velocity vectors (left) b) Blade element forces as a function of the aerodynamic forces and*
 115 *inflow angle (right)*

116 BEMT assumes that the change in momentum of each annular ring is solely accountable from the
 117 hydrodynamic forces on the corresponding blade elements (Burton et al. 2011). Hence the axial and
 118 tangential force equations from each theory are equated, giving expressions for calculating axial and
 119 tangential induction factors:

$$\frac{a}{(1-a)} = \frac{\sigma_r (C_L \cos \phi + C_D \sin \phi)}{4 \sin^2 \phi}$$

eq. 7

$$\frac{a'}{(1+a')} = \frac{\sigma_r (C_L \sin \phi - C_D \cos \phi)}{4 \sin \phi \cos \phi}$$

eq. 8

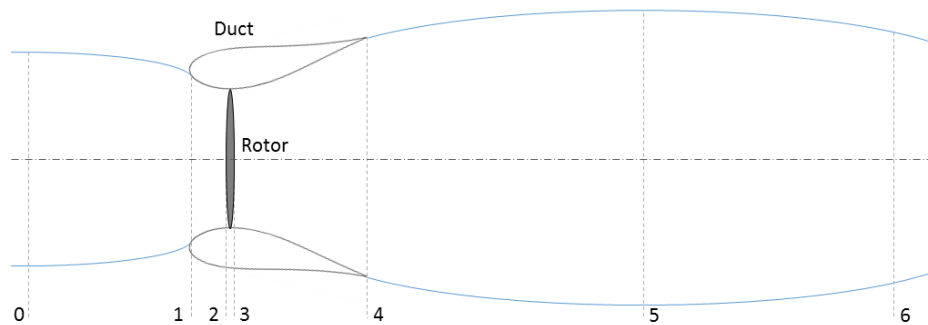
120 Where $\sigma_r = Bc/2\pi r$ is the local blade solidity. As the aerofoil coefficients vary non-linearly with
 121 angle of attack, these equations must be solved iteratively.

122 As the method neglects radial interactions, and considers only flow in the control volume, the
 123 approach is limited when considering physical phenomena such as vortex shedding and mixing with
 124 free stream fluid. Various correction factors can be applied to equations 7 and 8 to account for these
 125 effects, which are described in Sections 2.4 and 2.5.

126 2.2 Ducted BEMT

127 The incorporation of a duct aims to direct more flow through the turbine, and hence increase the
 128 momentum available for extraction. This is achieved by forcing of expansion in the diffuser reduces
 129 the pressure downstream, which augments the flow at the throat and results in a higher mass flow

130 rate. The presence of the structure alters the flow profile as shown in Figure 2-4, which makes the
 131 momentum equations based on the previous stream tube assumption unsuitable.



132

133 *Figure 2-4 Schematic of ducted turbine incorporating the actuator disc bounded by a stream tube, with numbers*
 134 *corresponding to sections in which areas, pressures and velocities are taken, consisting of: 0 – inflow upstream; 1 – duct*
 135 *inlet; 2 – actuator disc upstream; 3 – actuator disc downstream; 4 – duct outlet; 5 – wake downstream; 6 – wake far*
 136 *downstream*

137 The effects of the duct can be categorised by four main factors: i) the diffuser ratio (ratio of outlet
 138 area to throat area); ii) the flow separation within the diffuser; iii) the back pressure reduction at the
 139 exit and iv) the associated viscous losses (van Bussel 2007).

140 An analytical model devised by (Lawn 2003) relates the change in velocity using Bernoulli's equations
 141 to the change in pressure at various locations along the streamtube. These can be expressed in
 142 terms of the inlet efficiency (η_{02}), diffuser efficiency (η_{34}) and base pressure coefficient ($C_{p,b}$) by the
 143 following:

$$\eta_{02} = \frac{p_2 - p_0}{\frac{1}{2}\rho(U_0^2 - U_2^2)}, \quad \eta_{34} = \frac{p_4 - p_3}{\frac{1}{2}\rho U_3^2 \left(1 - \frac{A_3^2}{A_4^2}\right)}, \quad C_{p,b} = \frac{p_0 - p_4}{\frac{1}{2}\rho U_0^2}$$

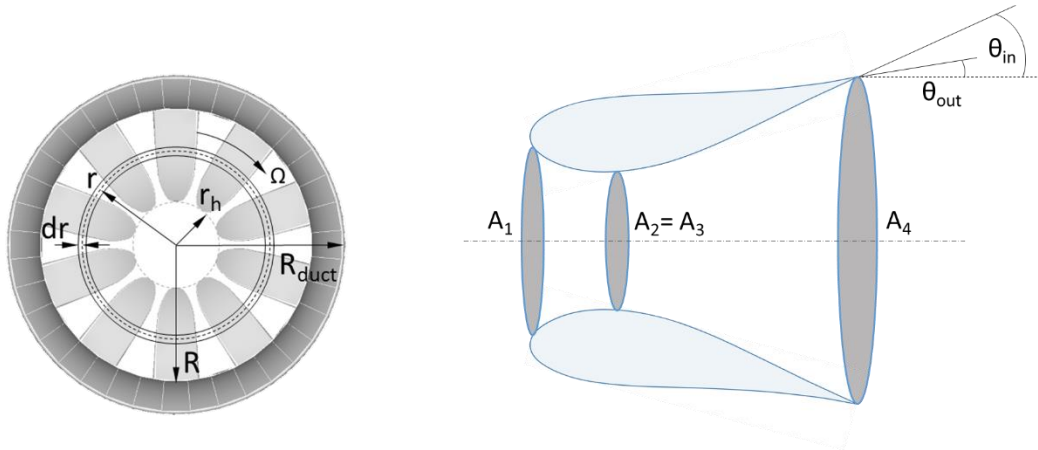
eq. 9

eq. 10

eq. 11

144 Experimental measurements or CFD results are then required to solve these equations. This
 145 framework is adopted by (Shives & Crawford 2011), where efficiencies are quantified using RANS
 146 simulations incorporating an actuator disc representation of the rotor. Several geometries of
 147 unidirectional ducts are analysed based on NACA0015 aerofoil shapes (Abbott & Von Doenhoff

148 1959), with varying geometrical parameters of: inlet contraction ratio (A_1/A_3); the diffuser expansion
 149 ratio (A_4/A_3); inner and outer diffuser surface angles (θ_{in} and θ_{out}), as shown in Figure 2-5.



150

151 *Figure 2-5 Figure 2 5 Ducted turbine a) rotor split into annular rings (left) and b) definition of geometrical parameters (right)*

152 Empirical approximations of the analytical expressions are then derived by (Shives & Crawford 2011),
 153 based on the CFD results. The inlet efficiency (η_{02}) was found to be within 5% of unity for all
 154 geometries considered, and therefore taking an efficiency of 100% was considered to have a
 155 negligible effect on the overall rotor forces. The diffuser efficiency can be written in terms of duct
 156 geometry, to characterise flow separation within the duct:

157
$$\eta_{34} = a_1 + b_1 \left(\frac{A_3}{A_4} \right) + c_1 \theta_{in} + d_1 \left(\frac{A_1}{A_2} \right)$$

158 *eq. 12*

159 Where $A_i = \pi R_i^2$ is the area at various positions along the stream tube (m^2). Similarly, the base
 160 pressure coefficient caused by obstruction of the flow is determined by:

161
$$C_{p,b} = a_2 + b_2 \left(\frac{A_3}{A_4} \right) + c_2 \theta_{out} + (d_2 + e_2 \theta_{out}) C_T + f_2 C_T^2$$

162 *eq. 13*

163 Where all coefficients are found using a least squares optimisation, summarised in Table 2-1.

164 *Table 2-1 Coefficients for empirical expressions of diffuser efficiency and base pressure coefficient, from (Shives & Crawford*
 165 *2011)*

a ₁	b ₁	c ₁	d ₁	a ₂	b ₂	c ₂	d ₂	e ₂	f ₂
0.8867	0.5212	-0.0108	-0.1313	0.2701	-0.333	0.0269	0.1068	-0.0152	-0.1275

166 The pressure change through the diffuser can be defined using the continuity equations, such that
 167 the coefficient of pressure between positions 3 and 4 can be written:

$$168 \quad C_{p,34} = \frac{p_4 - p_3}{\frac{1}{2}\rho U_3^2} = \eta_{34} \left(1 - \frac{A_3^2}{A_4^2} \right)$$

169 *eq. 14*

170 And the axial induction factor can finally be calculated using the following equation, where wake
 171 swirl is neglected:

$$172 \quad 1 - a = \sqrt{\frac{\eta_{02} - C_{Ti} + C_{p,b}}{\eta_{02} - C_{p,34}}}$$

173 *eq. 15*

174 The empirical/ analytical model is validated against power and thrust curves generated with CFD on
 175 three additional validation duct geometries, where reasonable agreement is seen.

176 2.3 Rotor power and thrust

177 Once axial and tangential induction factors are converged, coefficients of power (C_p) and trust (C_T)
 178 for the rotor are calculated to present non-dimensionalised turbine properties for comparative
 179 studies. These are often presented as a variation against the tip speed ratio (TSR), defined as:

$$C_T = \frac{\sum_{r_{hub}}^R dT}{\frac{1}{2}\rho A U_0^2} \quad , \quad C_p = \frac{\sum_{r_{hub}}^R dQ\Omega}{\frac{1}{2}\rho A U_0^3} \quad , \quad TSR = \frac{\Omega R}{U_0}$$

eq. 16

eq. 17

eq. 18

180 Where $A = \pi R^2$ is the area of the disc (m^2), or $A = \pi R_{duct}^2$ in the case of the ducted turbine.

181 Comparisons of bare and ducted turbines have previously been assessed using the rotor diameter
182 (Hansen 2008). In order to fairly compare the same relative areas, the RANS BEM study takes the
183 area at the duct inlet, and neglects the open centre, as explained by (Belloni et al. 2016). Although
184 this is not the objective of the present study, these definitions are used in order to gain directly
185 comparable results for validation. The tip speed ratio is defined in all cases using the rotational
186 velocity at the outer radius of the rotor, despite the fact that the blades are connected at either end
187 in the ducted case. In addition, the thrust coefficient at the local elements can be calculated as:

$$C_{T,loc} = \frac{T}{\frac{1}{2} \rho A_{rotor} U_d^2}$$

189 *eq. 19*

190 2.4 Tip and hub losses

191 Radial movement of fluid occurs at the blade tips and at the hub, as it is drawn from the pressure to
192 the suction side of the rotor. Due to the 2-dimensional nature of the blade element and momentum
193 methods, this movement is not accounted for directly in the theory and therefore has to be included
194 through an alternative method. Although exact solutions such as proposed by Bessel and Biot-
195 Savart, the issues arise with integrating into the BEMT method (Burton et al. 2011). The Prandtl
196 approximation solution yields a relatively simple analytical function which has been previously
197 employed to account for the effects of the tip losses (Chapman et al. 2013), and is easily
198 implemented into BEMT. Flow shedding at the blade tips leads to rotating helical structures in the
199 wake, which Prandtl conceptualises as a succession of discs travelling at a velocity between the free
200 stream and the wake (Burton et al. 2011). The loss factor can approximate the reduction in
201 hydrodynamic efficiency at the tip, and be expressed in the closed solution form proposed by
202 Prandtl:

$$F_{tip} = \frac{2}{\pi} \cos^{-1} e^{-f_{tip}}$$

204 *eq. 20*

205 Where the tip exponential term can be expressed:

$$206 \quad f_{tip} = \pi \left(\frac{R_w - r}{d} \right)$$

207 *eq. 21*

208 Where $R_w - r$ is the distance from the wake edge and d is the normal distance between successive
209 vortex sheets. This distance is related to the flow angle ϕ_s and the number of vortex sheets
210 intertwining from B number of blades:

$$211 \quad d = \frac{2\pi R_w}{B} \sin \phi_s = \frac{2\pi R_w}{B} \frac{U_0(1-a)}{W_s}$$

212 *eq. 22*

213 Taking the resultant wake velocity $W_s = \sqrt{(U_0(1-a))^2 + (\Omega r)^2}$ and taking the Glaert
214 adjustment such that $\frac{R_w}{W_s} \approx \frac{r}{W}$ (Masters et al. 2011):

$$215 \quad F_{tip} = \frac{2}{\pi} \cos^{-1} e^{-\frac{B}{2} \frac{R-r}{r} \frac{1}{\sin \phi}}$$

216 *eq. 23*

217 A similar expression is also suggested to account for losses at the hub (Moriarty & Hansen 2005):

$$218 \quad F_{hub} = \frac{2}{\pi} \cos^{-1} e^{-\frac{B}{2} \frac{r-r_h}{r_h} \frac{1}{\sin \phi}}$$

219 *eq. 24*

220 These can then be combined as an overall loss correction factor defined by:

$$221 \quad F = F_{tip} F_{hub}$$

222 *eq. 25*

223 The combined tip/ hub loss factor can then be input directly as a multiplication factor into the
224 expressions (Chapman et al. 2013) for thrust and torque from momentum theory (eq. 1 and eq. 2)
225 such that:

$$dT = 4\pi\rho U_0^2 a(1-a)rdrF \quad , \quad dQ = 4\pi\rho a'\Omega U_0(1-a)r^3 drF$$

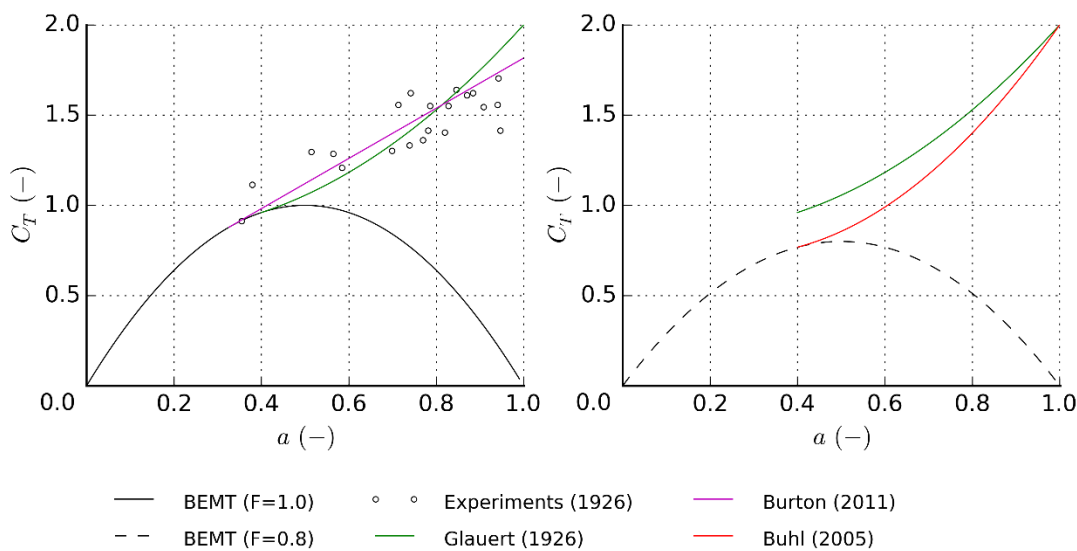
eq. 26

eq. 27

226 Axial and tangential forces from blade element theory are derived from aerodynamics equations, so
 227 remain unchanged.

228 2.5 Highly loaded conditions

229 At high axial induction factors, thrust forces are under predicted by the momentum equations as the
 230 stream tube representation does not account for interactions with the free stream fluid. For $a >$
 231 0.5 an unphysical reversal of flow in the wake is seen, from: $U_\infty = U_0(1 - 2a)$. In reality, turbulent
 232 mixing occurs with the free stream flow, injecting momentum into the slow moving fluid behind the
 233 turbine. Physical experiments with flat plates carried out by Glauert have shown much higher thrusts
 234 at axial induction factors above 0.4, as shown in Figure 2-6a.



236 *Figure 2-6 Thrust coefficient against axial induction factor, showing comparisons against BEMT with a) experimental values*
 237 *(points) and semi-empirical corrected values (left) and b) highly loaded corrected values with an arbitrary tip / hub loss of*
 238 *0.8 applied (right)*

239 Various best line fits to this data have been proposed, including a parabola proposed by Glauert
 240 (Burton et al. 2011) such that:

241 For $a \leq 0.4$:
$$C_T = 4a(1 - a)$$

242
$$\text{eq. 28}$$

243 For $a > 0.4$:
$$C_T = 0.889 - \frac{0.0203 - (a - 0.143)^2}{0.6427}$$

244 *eq. 29*

245 However, when combined with the tip/hub loss correction factor, a numerical instability occurs due
 246 to a gap at transition to the highly loaded regime (see Figure 2-6b). A solution as devised by Buhl
 247 (Buhl 2005) has previously successfully been implemented into BEMT (Chapman et al. 2013), which
 248 yields a smooth transition from the Glauert parabola to the prediction based on the axial
 249 momentum equations. Buhl reported reasonable agreement with the experimental data, as well as
 250 fixed boundary condition at $a=1$, analogous to a solid plate fully impeding flow.

251 For $a \leq 0.4$:
$$C_T = 4Fa(1 - a)$$

252 *eq. 30*

253 For $a > 0.4$:
$$C_T = \frac{8}{9} + \left(4F - \frac{40}{9}\right)a + \left(\frac{50}{9} - 4F\right)a^2$$

254 *eq. 31*

255 As these are relating to the overall rotor, we can implement this back to the momentum equations
 256 to write expressions for each annular ring as:

257 For $a \leq 0.4$:
$$dT = 4\pi\rho U_0^2 a(1 - a)rdrF$$

258 For $a > 0.4$:
$$dT = \pi\rho U_0^2 \left(\frac{8}{9} + \left(4F - \frac{40}{9}\right)a + \left(\frac{50}{9} - 4F\right)a^2\right)rdr$$

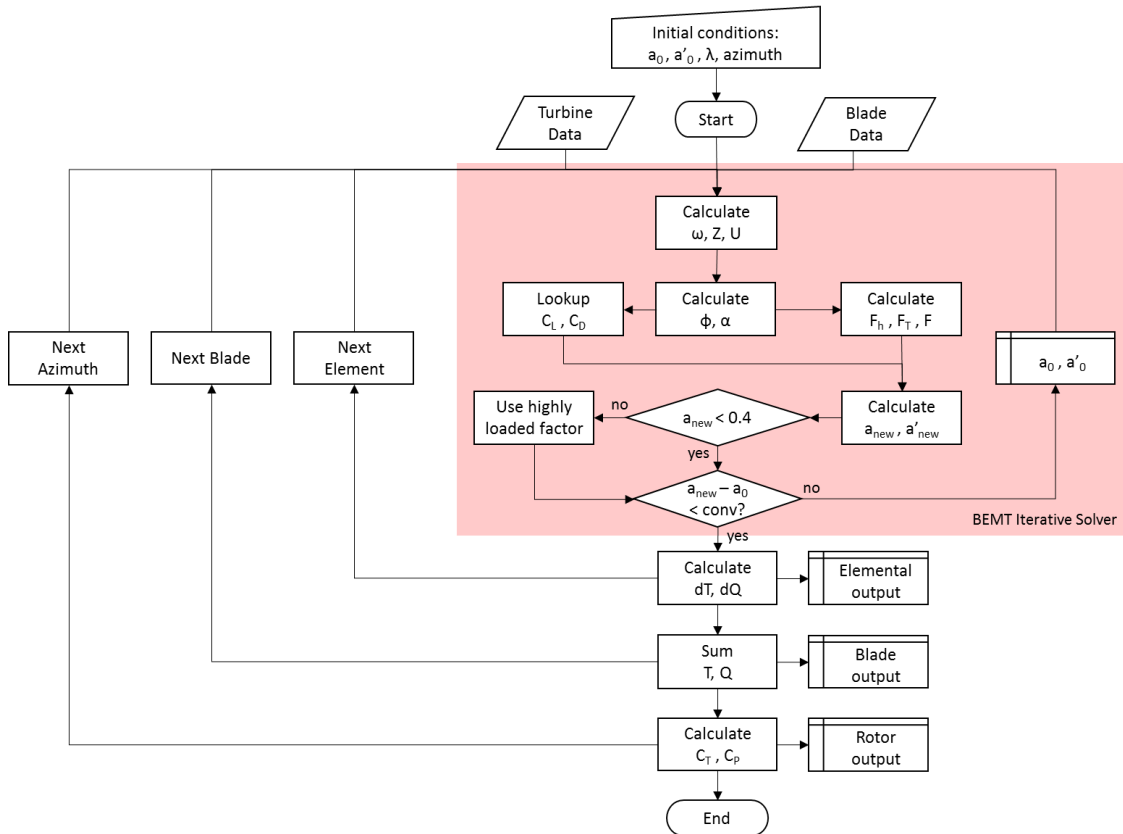
259 *eq. 32*

260 3 Model setup and input definitions

261 This section addresses the implementation of the BEMT into the code and defines the various input
 262 data for the validation cases. Sections 3.1 and 3.2 describe the BEMT code structure for the
 263 conventional, 3-bladed case and the ducted open centre case respectively. Sections 3.3 and 3.4
 264 detail the process of generating aerofoil coefficients, followed by the definition of other input
 265 parameters for the conventional and ducted validation cases in Sections 3.5 and 3.6 respectively.

266 3.1 Numerical implementation

267 The BEMT equations are solved iteratively with a programme written in Python. The overall code
 268 structure that has been utilised in the work presented in this paper is shown in Figure 3-1.



269
 270 Figure 3-1 General BEMT code structure implemented in Python

271 Here the convergence shown is based purely on the axial induction factor, however this is improved
 272 to include both axial and tangential induction factors in the convergence criteria. The iterations are
 273 performed using a minimisation package, an objective function similar to that of *fmincon* within
 274 Matlab, used in other codes (Masters et al. 2011; Shives 2011). The thrust and torque from each
 275 theory is considered equal, therefore the values from momentum and blade element can be
 276 rearranged and summed to equal the minimisation value (*g*):

$$g = (dT_1 - dT_2)^2 + (dQ_1 - dQ_2)^2$$

278 eq. 33

279 To implement the highly loaded condition:

280 For $a \leq 0.4$:

$$281 \quad g = \left(4\pi U_0^2 a(1-a)rF - \frac{1}{2}W^2 Bc(C_L \cos \phi + C_D \sin \phi) \right)^2$$
$$282 \quad + \left(4\pi a' \Omega U_0(1-a)r^2 F - \frac{1}{2}W^2 Bc(C_L \sin \phi - C_D \cos \phi) \right)^2$$

283 *eq. 34*

284 For $a > 0.4$:

$$285 \quad g = \left(\pi U_0^2 r \left(\frac{8}{9} + \left(4F - \frac{40}{9} \right) a + \left(\frac{50}{9} - 4F \right) a^2 \right) - \frac{1}{2}W^2 Bc(C_L \cos \phi + C_D \sin \phi) \right)^2$$
$$286 \quad + \left(4\pi a' \Omega U_0(1-a)r^2 F - \frac{1}{2}W^2 Bc(C_L \sin \phi - C_D \cos \phi) \right)^2$$

287 *eq. 35*

288 Where each part is squared to avoid convergence to an incorrect solution.

289 The *minimise* function within SciPy offers a variety of optimisation algorithms, which can be selected
290 based on the nature of the problem (SciPy Community 2016). In this case, the Sequential Least
291 Squares Programming (SLSQP) gave the best compromise between running time, convergence and
292 operational constraints. A maximum iteration limit was set to 1000, and a tolerance for the value g
293 of 1.0E-10. Boundary constraints were set to ensure that induction factors stay within reasonable
294 limits, where tangential values being less than 0.5, and axial between -0.9 to 0.9.

295 3.2 Duct model implementation

296 The same minimise objective function is applied, however the minimisation value is defined as:

$$297 \quad g = \left((\eta_{02} - CT_i + C_{pb} - (\eta_{02} - C_{P34}))(1-a)^2 \right)^4$$
$$298 \quad + \left(4\pi a' \Omega U_0(1-a)r^2 F - \frac{1}{2}W^2 Bc(C_L \sin \phi - C_D \cos \phi) \right)^4$$

299 *eq. 36*

300 Here the highly loaded condition is not included, as the axial induction factor never converges on
301 $a > 0.4$. The equation now incorporates the axial induction factor expression from the duct

302 analytical / empirical model as defined in eq. 15, and thrust coefficient C_{Ti} calculated from the blade
303 element theory using eq. 5. The thrust and torque sides are increased to the power 4 in this case, as
304 it was discovered to have a higher stability. The iterative loop steps through the induction factors
305 searching for equilibrium between the momentum and blade element theories, in order to satisfy
306 the minimisation condition (g). The higher stability is thought to be achieved with the larger
307 exponent value due to smaller increments imposed when the approaches the equilibrium value. This
308 increases the number of steps taken to reach convergence, however does not noticeably affect the
309 running time.

310 Where available, the duct geometry is taken directly from the reference (Belloni et al. 2016),
311 including duct inlet and outlet radii. The inlet and outlet diffuser surface angles required by the
312 analytical model are not given, and not easily defined for a bi-directional ducts. A calibration study
313 was thus performed to estimate appropriate values, by applying the model to a commercial open
314 centre device, and comparing the corresponding thrust and power curves with blade resolved CFD
315 simulations. Appropriate values were determined as: $\theta_{in} = 30^\circ$ and $\theta_{out} = 10^\circ$.

316 Due to the configuration of blade tips being connected, the formation of tip vortices is restricted,
317 which has implications on the tip-losses seen in classical turbines. CFD studies have reportedly
318 shown that the change in axial velocity at the tip is small (Fleming & Willden 2016) and therefore the
319 tip loss factor is set to unity.

320 For this case, an open centre hub is incorporated, connecting the ends of the blades at the centre.
321 This is thought to constrain the vortex shedding which is the basis of the Glauert hub loss, and
322 therefore is assumed to be unity in this case. This is a limitation of the model, as the complex nature
323 of the flow in this region is thought to have associated 3 dimensional effects and therefore
324 associated hydrodynamic efficiency losses. An alternative correction factor is currently being sought,
325 however due to the additional complexity in the mixing with flow through the open centre, requires
326 extensive blade resolved CFD studies.

327 3.3 Aerofoil coefficients

328 Aerofoil characteristics are required in determining the element aerodynamic forces, which can be
329 obtained directly from catalogued data such as (Abbott & Von Doenhoff 1959) which are based on
330 wind tunnel experiments at specific Reynold's numbers. XFOIL is an alternative method: a Fortran
331 based programme incorporating a linear vorticity function panel method with a viscous boundary
332 layer and wake model (Drela 1989). For NACA profiles not contained within the XFOIL database,
333 surface ordinates are obtained from catalogued data (UIUC Applied Aerodynamics Group 2015) and
334 prescribed, along with the chord based Reynolds number as:

$$335 \quad Re_{ch} = \frac{\rho c W}{\mu}$$

336 *eq. 37*

337 Where $W = \sqrt{U_0^2 + (\Omega r)^2}$ denotes the resultant velocity over the surface of the aerofoil (ms^{-1}) and
338 μ is the dynamic fluid viscosity (Nsm^{-2}). Small changes in Reynold's number were found to have an
339 insignificant on the overall rotor performance, and therefore the rotational velocity is taken at the
340 optimal performance of the turbine. As the Viterna extraoplation function uses chord and thickness
341 values at 75% down the length of the blade (Ning 2013), it seems reasonable to use the same
342 location in Reynolds number calculation.

343 Aerofoil coefficients for the bare 3-bladed turbine uses XFOIL generated data (at $Re_{ch} = 3.0E+05$),
344 whereas the ducted case takes catalogued data (at $Re_{ch} = 1.5E+06$).

345 3.4 Corrections to aerofoil coefficients

346 As XFOIL calculations and experiments are based on 2D static wind tunnel measurements, the 3D
347 nature of flow due to the rotation of the blade is not accounted for. In reality, radial forces in the
348 fluid induce a Coriolis Effect, acting in the direction of the trailing edge which effectively delays the
349 onset of boundary layer separation. This delayed stall phenomenon varies as a function of chord and

350 radius, and can be accounted for by applying a Du-Selig (Tangler & Selig 1997) model to the lift
351 coefficients, and an Eggers (Hansen 2004) adjustment to the drag.

352 As a result of BEMT iteratively solving for inflow angle, data for large range of angles of attack is
353 required, in some cases exceeding the point of stall, which is beyond the capabilities of XFOIL. Values
354 in these conditions can be generated using an extrapolation function as proposed by Viterna
355 (Viterna & Janetzke 1982), using the aerofoil aspect ratio 75% down the length of the blade.

356 3.5 Classical bare turbine properties

357 Validation of the classical BEMT model for bare turbines is performed against 1/20th scale model
358 experiments (Batten et al. 2006). The 3-bladed turbine has a rotor radius (R) of 0.4m, and tests are
359 performed in a fully enclosed cavitation tunnel. Radial distribution of blade chord (c), thickness (t)
360 and twist (β) are detailed in Table 3-1.

361 *Table 3-1 1/20th scale turbine properties showing distributions with normalised radius (Bahaj et al. 2007)*

r/R	β (°)	c/R	t/c (%)
0.20	15.0	0.125	24.0
0.30	9.5	0.116	20.7
0.40	6.1	0.106	18.7
0.50	3.9	0.097	17.6
0.60	2.4	0.088	16.6
0.70	1.5	0.078	15.6
0.80	0.9	0.069	14.6
0.90	0.4	0.059	13.6
1.00	0.0	0.050	12.6

362 Three flow rates and turbine configuration are considered:

Parameter	Case 1	Case 2	Case 3
Inflow velocity (m/s)	1.73	1.54	1.3
Blade pitch (°)	5	10	12

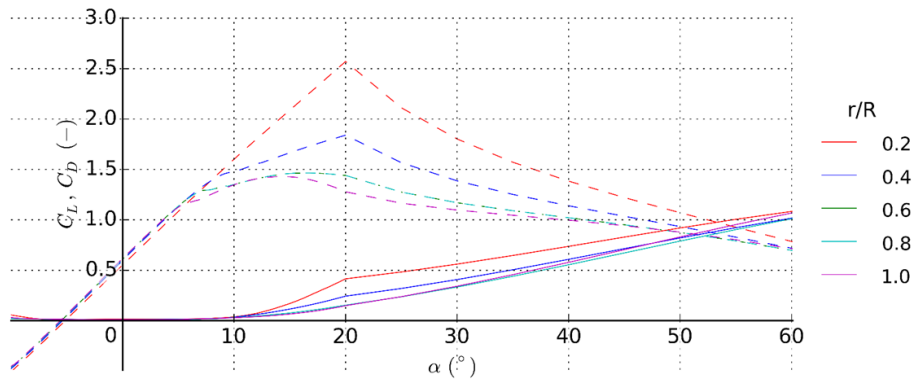
364 The flow through the water column under experimental conditions is inherently unsteady and non-
 365 uniform, combined with complex interactions with the surrounding walls. The blockage ratio of the
 366 experimental setup is 17%, and results are quoted by the author in their blockage corrected form
 367 (Bahaj et al. 2007). As tests are run in a cavitation tunnel, there are no free surface effects. Within
 368 the BEMT, the inflow is assumed as a steady and ‘frozen’, where in this analysis a shear profile is
 369 incorporated in order to approximate the effects of bottom friction as a 1/7th power law:

$$370 \quad U_0 = U_{hub} \left(\frac{z}{z_{hub}} \right)^{\frac{1}{7}}$$

371 *eq. 38*

372 Where U_{hub} is the average flow velocity at the hub height (ms^{-1}), z is the height of the element above
 373 the seabed (m) and z_{hub} is the height of the hub above bottom, taken as 0.6m. z is calculated as a
 374 function of the blade azimuth and element radial location and inserted in the above equation to
 375 determine the inflow velocity for each element. This velocity is then used in the BEMT loop, where
 376 an azimuth stepping function is applied. Rotor power and thrust coefficients are then determined by
 377 taking the average axial and tangential forces over one turbine rotation.

378 The blade profile consists of NACA63-8xx aerofoil sections, xx being the thickness to chord ratio. The
 379 lift and drag coefficients against angle of attack for a Reynolds number of 3.0E+05 (corresponding to
 380 1.73 ms^{-1} inflow velocity) are shown in Figure 3-2, generated using XFOIL. Values are 3D stall delay
 381 corrected as a function of location along the blade, and extrapolated past stall condition.

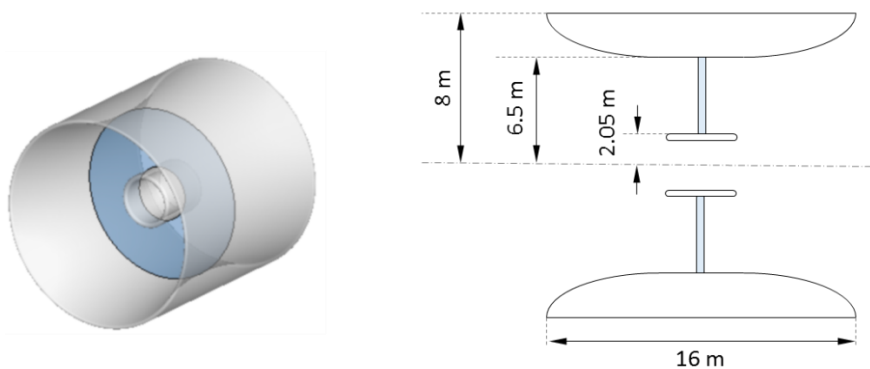


382

383 *Figure 3-2 Coefficient of lift (dashed lines) and drag (solid lines) against angle of attack for NACA63-8xx profiles for various*
 384 *normalised radii, at a Reynold's number 3.0E+05*

385 3.6 High solidity, ducted, open-centre turbine properties

386 To assess the performance of the duct BEMT model, comparisons are made against a coupled RANS
 387 BEM study of a bidirectional ducted and open centre turbine. This is based on full scale geometry,
 388 with general dimensions of duct radius (R_{duct}), rotor radius (R_{rotor}) and hub radius (R_{hub}) given in
 389 Figure 3-3. Values of inlet and outlet angles (indicated in Figure 2-5) are calibrated with the blade
 390 resolved CFD studies, where $\theta_{in} = 30^\circ$ and $\theta_{out} = 10^\circ$ show the best representation. A sensitivity
 391 analysis of these parameters is shown in Section 5.6.



392

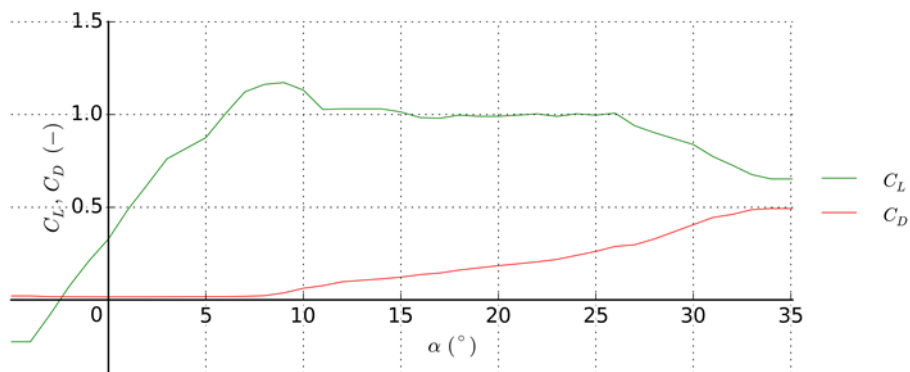
393 *Figure 3-3 Ducted open centre turbine overall dimensions (Belloni et al. 2016)*

394 The number of blades, aerofoil chord lengths and thicknesses are incorporated into values of solidity
 395 (σ_r), where radial distributions are detailed in Table 3-3.

396 *Table 3-3 Ducted and open centre turbine properties variation with normalised radius. Data reproduced from (Belloni et al.*
 397 *2016)*

r/R	β (°)	σ_r
0.30	29.7	0.420
0.40	25.6	0.305
0.50	20.8	0.220
0.60	17.2	0.163
0.70	14.2	0.124
0.80	12.0	0.100
0.90	10.3	0.083
1.00	8.4	0.070

398 One flow condition is considered, based on a uniform inflow with no bottom friction, at a constant
399 velocity of 2ms^{-1} . This has a corresponding chord based Reynolds number of approximately $1.0\text{E}+06$.
400 The blades consist of Risø-A1-24 aerofoils, with lift and drag coefficients as shown in Figure 3-4,
401 taken from wind tunnel data at a Reynolds number of $1.6\text{E}+06$ (Fuglsang et al. 1999) . These raw
402 values are directly applied to the mode, with no 3D correction implemented, to be consistent with
403 the validation methodology (Belloni 2013). No extrapolation function is used, where if $\alpha < 5^\circ$, C_L and
404 C_D are equal to those at $\alpha = 5^\circ$. Additionally, for $\alpha > 35^\circ$, C_L and C_D are equal to those at $\alpha = 35^\circ$.



405

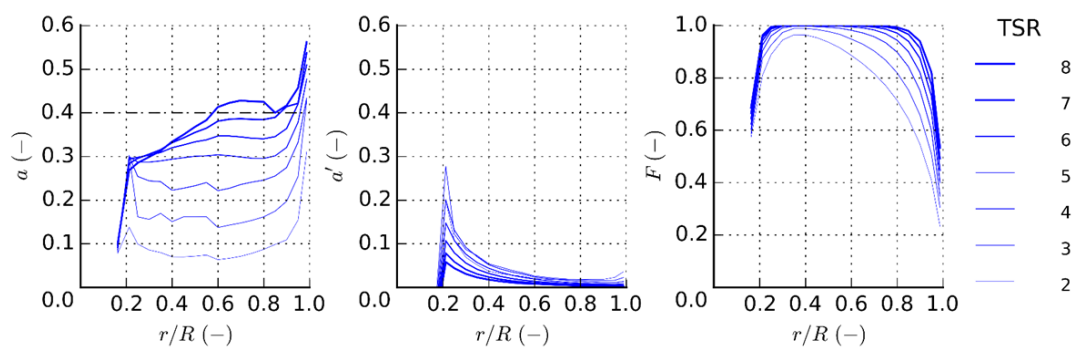
406 *Figure 3-4 Coefficients of lift and drag against angle of attack for Riso-A1-24 aerofoil under a Reynold's number $1.6\text{E}+06$*
407 *(Fuglsang et al. 1999)*

408 4 Results

409 This section presents the results of the two BEMT models and compare them with various validation
410 data from the literature. Section 4.1 gives the comparison of the conventional 3-bladed case with
411 previous scale model experimental data. Sections 4.2 and 4.3 present the results of the ducted BEMT
412 compared to a coupled RANS-BEM model, where overall rotor performance as well as span-wise
413 variations are shown.

414 4.1 Classical bare turbine validation

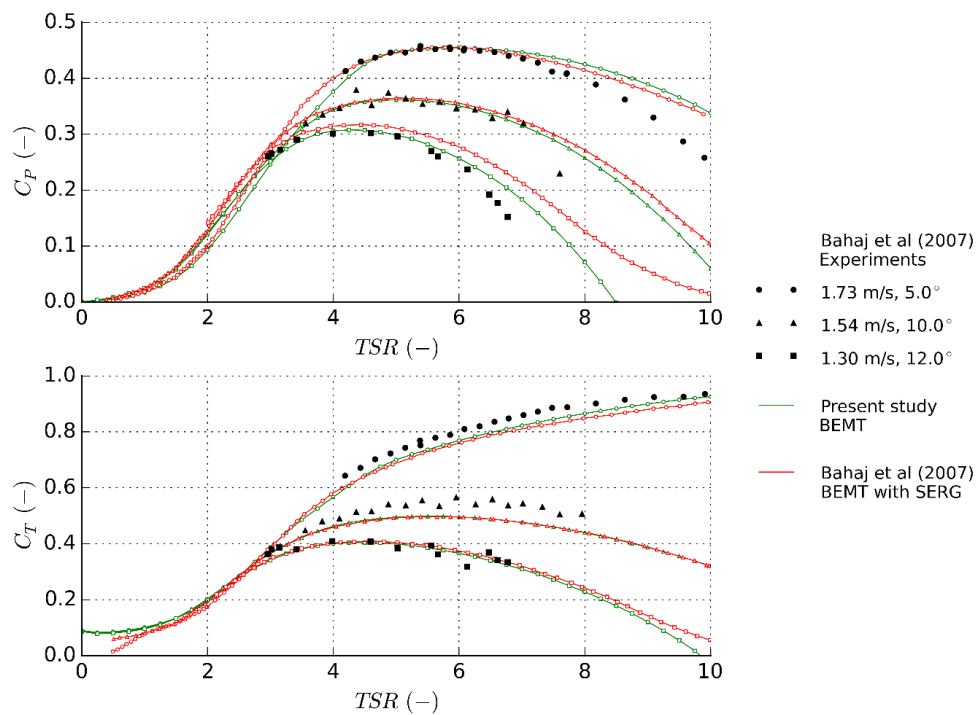
415 Using the described input data, the model is run for each individual inflow velocity and pitch.
416 Intermediate calculation steps are inspected in order to assess the model performance, to ensure
417 convergence is well established and to gain indications of magnitude and location at which
418 correction factors are being applied. Figure 4-1 shows the distribution of axial and tangential
419 induction factors as well as the tip/hub loss correction factor along the blade length for an inflow
420 velocity of 1.73ms^{-1} . The axial induction factor is seen to exceed the transition to the highly loaded
421 regime only at this inflow, occurring mainly at the blade tips except for at a TSR of 8. The tip/hub loss
422 describes the reduction in hydrodynamic efficiency along the blade, becoming more influential
423 towards the tip and hub as per its definition. The magnitude of this efficiency decreases with TSR,
424 where the tip losses are clearly more significant in all cases considered. For the lowest TSRs, the
425 correction can be seen to apply along the entire length of the blade.



426

427 *Figure 4-1 a) axial induction factor (left), b) tangential induction factor (middle) and c) tip/hub correction factor (right)*
428 *variation with normalised radius at various tip speed ratios, for inflow of 1.73ms^{-1} , pitch 5, taken at an azimuth of 0°*

429 Figure 4-2 shows the power and thrust curves for the turbine, comparing measured and numerical
 430 data. Overall trends are similar for each inflow: levels generally increase to a peak at an optimal TSR,
 431 the largest corresponding to the highest inflow. For the most part, results from the BEMT models
 432 show excellent agreement with the experimental data. Inter comparison of the numerical models
 433 also shows very similar trends, with little divergence in the power at the lowest inflow velocity.
 434 Regions of over prediction in power are evident towards the higher TSRs. This is potentially caused
 435 by the large blockage correction factor applied to the experimental data.



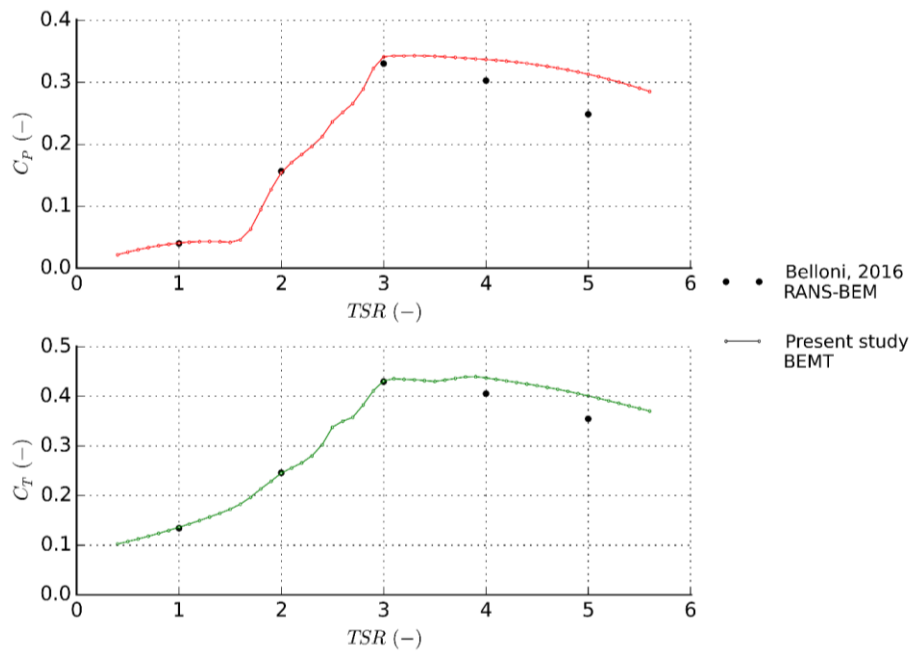
436
 437 *Figure 4-2 Coefficient of power (top) and thrust (bottom) variation with tip speed ratio for 1/20th scale classical bare turbine*
 438 *for velocities and blade pitches: 1.73ms⁻¹, 5°; 1.54ms⁻¹, 10°; and 1.3ms⁻¹, 12°. Comparing experimental data with BEMT*
 439 *results from present study and with University of Southampton (SERG)*

440 4.2 Ducted rotor performance and thrust

441 The axial induction factor for all cases is found to be below the transition to the highly loaded regime
 442 for all TSR, so no highly loaded correction factor is applied.

443 Figure 4-3 shows the coefficient of power and thrust, which again follows an increasing trend up to a
 444 maximum at an optimal TSR. Comparison of the ducted BEMT results with RANS-BEM shows
 445 exceptional agreement, particularly up to the optimal at 3.0. Beyond the peak, a divergence is seen

446 between the datasets, where ducted BEMT calculates up 25% higher in power and 13% in thrust at
447 TSR 5.

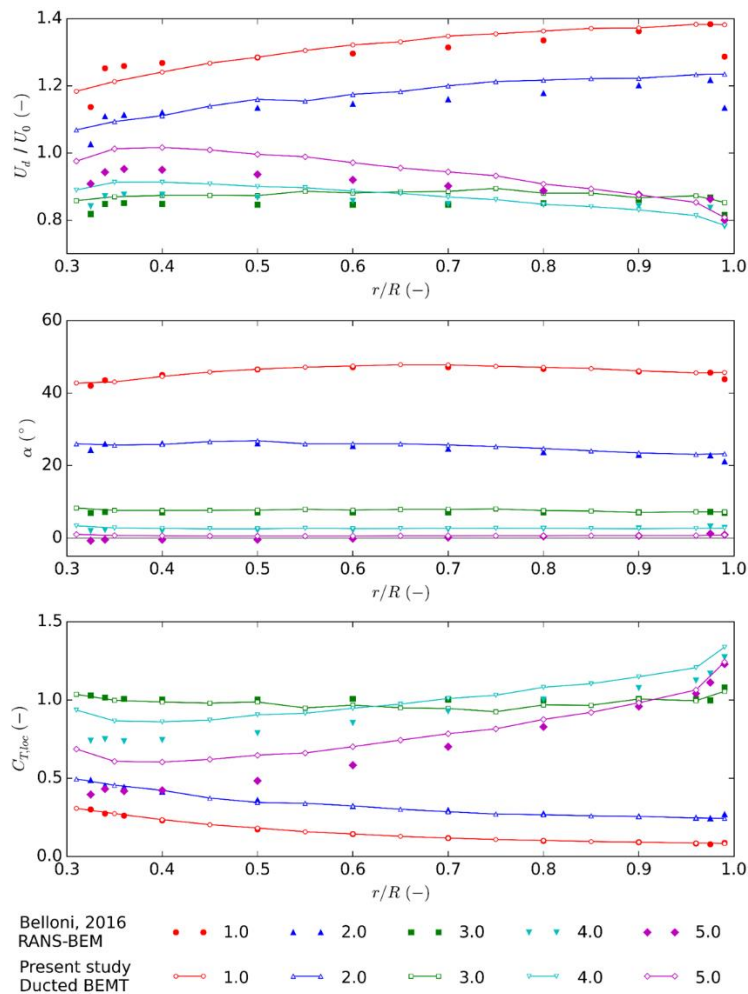


448

449 *Figure 4-3 a) coefficient of power (top) and b) thrust (bottom) variation with tip speed ratio for full scale open centre and*
450 *ducted turbine, comparing present ducted BEMT with RANS-BEM results*

451 4.3 Ducted rotor blade distribution

452 Rotor averaged values give an overall indication to the performance of a turbine, however it is also
453 important to be able to assess the force distributions along the blade length, particularly when
454 performing loading and bending moments for structural assessments. Figure 4-4 shows the blade
455 distributions of certain parameters calculated in the model, namely the velocity at the disc, angle of
456 attack and local element coefficient of thrust. Comparing the ducted BEMT to RANS-BEM, excellent
457 agreement is seen for angles of attack at all TSRs considered, as well as for velocity and local
458 element thrust up to TSR 3. Some discrepancies are evident when inspecting the velocity and local
459 thrust at $TSRs$ 4-5. This is in accordance with the results for the entire rotor, but here we can identify
460 the divergences are located at blade elements towards the hub (for low r/R values).



461

462 *Figure 4-4 Variations of a) flow velocity at the disc divided by velocity at the inlet (top), b) angle of attack (middle) and c)*
 463 *local elemental thrust coefficient (bottom) with normalised radius for various tip speed ratios, comparing ducted BEMT*
 464 *(lines) with RANS-BEM (points)*

465 5 Discussion

466 Here we discuss the findings from the results, with Section 5.1 focussing on the validation of the
 467 classical code with a conventional turbine and Section 5.2 on the ducted BEMT model. Additional
 468 observations, model limitations, computational requirements and sensitivity to duct diffuser angles
 469 are then explored in Sections 5.3 – 5.6.

470 5.1 Validation and implementation of the BEMT method

471 It is seen that converged axial induction levels are below the transition to the highly loaded regime
 472 for the majority of calculations, except at the blade tips and at high TSRs outside of the optimal

473 operating conditions. Intermediate calculations of flow parameters show that convergence is fully
474 established within the model limits for each simulation.

475 The comparison of the classical BEMT model with the University of Southampton model (SERG)
476 results shows that the developed code presented here achieves a good implementation of the
477 theory. The models also show very good agreement with the experimental measurements of C_p and
478 C_T , with a slight tendency to over predict at higher TSR values. This is thought to be accounted for by
479 the blockage effects within the experimental set up. In engineering applications, these TSRs are of
480 less interest as they exceed the optimal operating conditions of the turbine. Further validation of the
481 code is carried out against additional experiments and are detailed in (Allsop et al. 2016).

482 5.2 Ducted BEMT comparison with RANS BEM

483 The overall values of rotor C_p and C_T are almost identical for TSRs below 4, which include the optimal
484 operating conditions.

485 Both methodologies make use of the blade element theory, using similar geometrical parameters,
486 aerofoil lift and drag coefficients and correction factors. The differences in the results from the two
487 studies are therefore purely a function of how the changes in fluid momentum are treated. As there
488 is good agreement seen between the results, the suggestion is that the momentum changes
489 calculated within the analytical ducted BEMT are very similar to those computed by the CFD model.
490 Further analysis of the radial distributions indicate the calculations are similar on an elemental level
491 and not only rotor averaged. Although this has positive implications for the approach taken, this is
492 not a comprehensive validation of the method and more representative of an early stage
493 qualification. In order to increase confidence in the method, further comparisons are recommended
494 ideally against higher fidelity blade resolved CFD.

495 Over predictions seen at higher TSRs are likely due to the more complex flow characteristics at these
496 conditions, which are better captured using the more detailed CFD. Assessment of the blade
497 distributions shows that the over predictions of disc velocity are located closer to the hub, with the

498 tips shows more reasonable correlation. This is thought to stem from flow interactions with the hub,
499 with fluid likely being drawn through the open-centre and therefore reducing the hydrodynamic
500 efficiency of the blade elements towards this region. As the model does not account for span wise
501 flow, the application of a hub-loss factor could be considered, based on further analysis of these
502 interactions.

503 5.3 Additional observations

504 Axial induction factors converge on values less than the transition point to the highly loaded regime,
505 therefore under the input conditions considered, the results are always solved as per the ducted
506 BEMT calculations. This shows a non-dependency on the Buhl correction factor, which has
507 associated uncertainties due to semi-empirical nature of the correction based on experiments with a
508 significant spread.

509 In order to remain consistent with the inputs of the RANS-BEM model, the lift and drag coefficients
510 at angles of attack above 35° are kept constant with the reason being that this is a rare occurrence at
511 non-optimal operating conditions. It is seen that for low TSR, the angles of attack are consistently
512 above this limit, and therefore a post stall model could be used such as the Viterna extrapolation
513 function which is commonly employed, in order to improve the accuracy of the aerodynamic
514 coefficients.

515 5.4 Computational requirements

516 Studies on conventional turbines quoted computational requirement of 100 CPU-hours per turbine
517 rotation using blade resolved RANS CFD and 12 CPU-hours for each simulation using coupled RANS-
518 BEM (McIntosh et al. 2012). No details on the computational set up is given by this reference.

519 The coupled RANS-BEM study was performed on a 16 node computer cluster, with 8 cores per node.
520 Steady computations were completed in 8 hours using 4 cores, equivalent to 32 core hours for each
521 of the 5 simulations (Belloni 2013).

522 The present ducted BEMT computations were performed using a laptop running an *Intel Core™ i5*
523 2.9 GHz dual core processor with 8 GB RAM. Simulations were completed within 3 minutes,
524 generating all 60 points on the power and thrust curves, equivalent to 6 core minutes.
525 Computational time from separate studies cannot be directly compared, due to dependencies on
526 factors such as the computer used, processor type, number of partitions and clock time. There are
527 also dependencies on certain CFD parameters such as the mesh definition, domain size and time
528 step used. However, differences of several orders of magnitude seen in this study is indicative of
529 substantial computational cost savings when using the current model. This highlights an advantage
530 in the application of performing engineering assessments such as fatigue damage or when making
531 multiple design iterations.

532 5.5 Model limitations

533 Both the ducted BEMT and RANS BEM models are based on the blade element theory restrictions,
534 where any span wise flow is not considered, and individual aerofoil sections are analysed as a
535 function of the lift and drag coefficients. In order to reduce the limitations of 2D analyses,
536 corrections for physical behaviour could be included, such as the delayed stall effects by applying the
537 Du-Selig and Eggers adjustments to lift and drag coefficients. However, the complex flow through
538 the different turbine configuration is likely to have impacts on the Coriolis Effects of flow, and would
539 need to be further analysed.

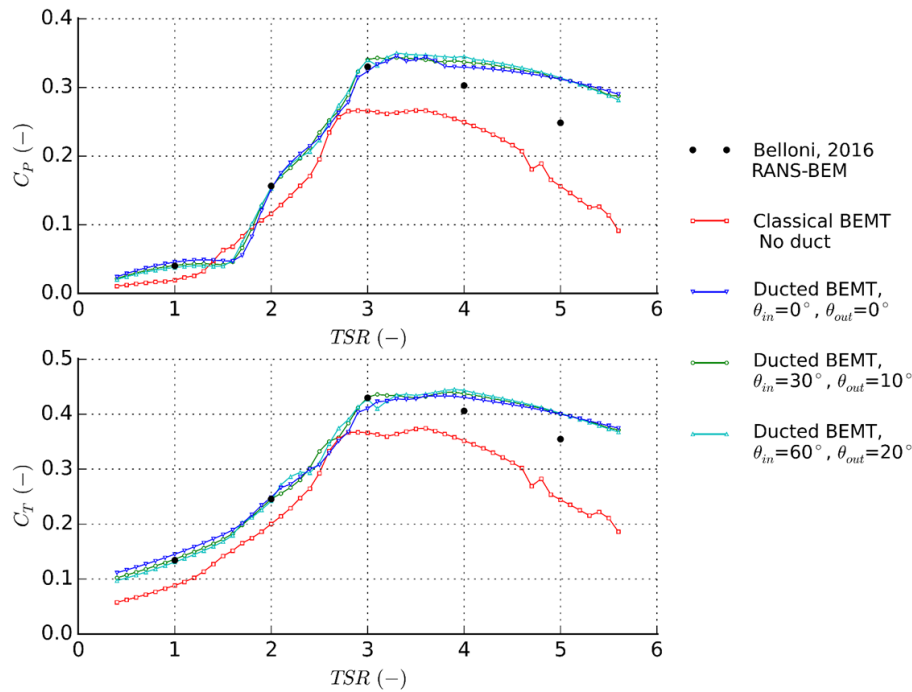
540 RANS has the ability to capture the spanwise flow, however this is beyond the capabilities of the
541 momentum equations which are based on independent annular rings, capturing no radial
542 interactions between elements. This is thought to be more significant around the open centre hub
543 geometry. As the bending stress is a function of all forces along the blade, this is thought to have
544 implications on blade life, and should be considered when feeding the loads into a structural
545 analysis.

546 The incorporation of the duct effects in the BEMT equations are devised from CFD studies of
547 unidirectional duct geometries. When applying this to the bi-directional duct in this case, the inlet
548 and outlet angles are less easy to define, yet are incorporated within the empirical expressions.
549 These angles were empirically calibrated using a separate study on an open centre device,
550 comparing the resultant C_p and C_T curves with blade resolved CFD studies. There are inevitably
551 inaccuracies with this approach due to the differences in the geometry of machines, as well as
552 calibrating against a methodology that models individual blades.

553 The BEMT model is unable to characterise the flow in the wake, and does not consider any mixing
554 with the fluid surrounding the stream tube. The present study only considers a flow direction
555 perpendicular to the rotor plane, however this could be adapted to additionally assess yaw. The flow
556 is also considered inviscid and steady and therefore does not account for dynamic effects such as
557 turbulence or inertia. Quasi static simulations can be performed, where frozen inflow conditions are
558 applied at each time step.

559 5.6 Sensitivity to duct model parameters

560 Additional simulations were performed in order to assess the effect of adding the duct correction, as
561 well as the impact the diffuser parameters has on the power and thrust predictions. Figure 5-1 **Error!**
562 **Reference source not found.** shows that the classical BEMT results are lower than those predicted
563 by the ducted BEMT for the majority of TSRs, as expected due to the flow augmentation effects.
564 Additionally, various duct parameters are tested, using: $\theta_{in} = 0^\circ / \theta_{out} = 0^\circ$ (as a low extreme), $\theta_{in} =$
565 $30^\circ / \theta_{out} = 10^\circ$ (as the reference values from a calibration study) and $\theta_{in} = 60^\circ / \theta_{out} = 20^\circ$ (as a high
566 extreme of twice the reference values from a calibration study). It can be seen that power and thrust
567 predictions using extreme values are within 5% of those when using the reference in this study,
568 indicating a small sensitivity to these parameters.



569

570 *Figure 5-1a) coefficient of power (top) and b) thrust (bottom) variation with tip speed ratio for full scale open centre and*
 571 *ducted turbine, comparing classical BEMT with Ducted BEMT with various diffuser parameters*

572 6 Conclusion

573 This study details a 'classical' BEMT model, developed for analysing power output and rotor thrust
 574 forces on 3-bladed, bare TSTs. The developed BEMT code is implemented and verified by comparing
 575 results to an academic code and proves being capable of representing physical effects with good
 576 agreement to scale model experimental measurements.

577 An analytical model which aims to characterise the effects of flow through a duct as a function of the
 578 inlet efficiency, diffuser efficiency and base pressure is considered. Empirical expressions for these
 579 parameters are formulated in the literature, based on CFD studies of various different unidirectional
 580 ducts, as functions of numerical coefficients and duct geometry. The empirical expressions are
 581 combined to formulate a new expression for the axial induction factor, which is incorporated into
 582 the BEMT iterative procedure. Due to the geometrical differences of a bidirectional duct, certain
 583 values are calibrated through applying the model using blade resolved CFD results.

584 The rotor power and thrust predicted by the ducted BEMT model is almost identical to a RANS BEM
585 study, for TSRs up to the optimal operating condition. As the blade element theory application is
586 consistent in each method, this suggests a similar computation of the momentum change from the
587 empirical expression and the CFD. This is further emphasised by similarities seen in the blade
588 distribution of flow velocity, angle of attack and local elemental thrust.

589 Some divergence is seen at higher TSRs, with differences up to 25% higher power and 13% higher
590 thrust compared to RANS BEM. These are a result of over predictions in the elemental flow velocity
591 close to the hub, thought to be due to the flow around the hub and through the open centre, which
592 are beyond the capability of the BEMT method to capture. A hub loss factor could be introduced to
593 approximate the reduced hydrodynamic efficiency in this region, however would require detailed
594 CFD analysis to ensure the complex flow interactions are well represented.

595 The ducted BEMT has shown significantly lower computational requirements compared with the
596 coupled RANS BEM method, in the order of a few minutes on a laptop rather than a few hours on a
597 computer cluster. This highlights the advantage of the model when multiple engineering
598 assessments are required in performing fatigue analyses, or when access to high performance /
599 clustered computational resources are restricted.

600 Despite the positive implications of these results, it should be noted that this study is not a
601 comprehensive validation of the method. Due to the limited number of data points for comparison,
602 this result is more representative only of an early stage qualification. Assessment against additional
603 cases, preferably with alternative models or experimental measurements should be performed to
604 form a more definitive conclusion.

605 As further and ongoing work, the presented model is being applied to commercial turbines, for
606 further validation against blade resolved CFD studies under several inflow velocities. Sensitivity
607 studies will also be performed on other duct parameters such as the inlet and diffuser ratios, to gain
608 a better understanding of the model dependencies. The model will then be extended to calculate

609 the associated stress distributions along the blade. The fast computation of this method will enable a
610 higher number of analyses to be performed with many different inflow parameters, and ultimately
611 used to predict blade fatigue damage.

612 7 Acknowledgments

613 This research is carried out as part of the Industrial Doctoral Centre for Offshore Renewable Energy
614 (IDCORE) programme, funded by the Energy Technology partnership and the RCUK Energy
615 programme (Grant number EP/J500847/1), in collaboration with EDF R&D. The authors would also
616 like to thank Optydro for supplying blade resolved CFD results, in order to calibrate the duct model.

617 8 References

- 618 Abbott, I.H. & Von Doenhoff, A.E., 1959. *Theory of Wing Sections (Including a Summary of Airfoil*
619 *Data)*, Langley: Dover Publications Inc, New York. Available at:
620 <http://www.journals.uchicago.edu/doi/10.1086/470266>.
- 621 Allsop, S. et al., 2016. A validated BEM model to analyse hydrodynamic loading on tidal stream
622 turbine blades. In *3rd Asian Wave and Tidal Energy Conference, 24-28 October 2016*. Singapore.
- 623 Bahaj, A.S. et al., 2007. Power and thrust measurements of marine current turbines under various
624 hydrodynamic flow conditions in a cavitation tunnel and a towing tank. *Renewable Energy*,
625 32(3), pp.407–426.
- 626 Batten, W.M.J. et al., 2007. Experimentally validated numerical method for the hydrodynamic design
627 of horizontal axis tidal turbines. *Ocean Engineering*, 34(7), pp.1013–1020.
- 628 Batten, W.M.J. et al., 2006. Hydrodynamics of marine current turbines. *Renewable Energy*, 31(2),
629 pp.249–256.
- 630 Belloni, C., 2013. *Hydrodynamics of Ducted and Open-Centre Tidal Turbines (PhD Thesis)*. The
631 University of Oxford.

632 Belloni, C., Willden, R.H.J. & Houlby, G., 2016. An investigation of ducted and open-centre tidal
633 turbines employing CFD-embedded BEM. *Renewable Energy*.

634 Buhl, M.L., 2005. *A New Empirical Relationship between Thrust Coefficient and Induction Factor for*
635 *the Turbulent Windmill State*,

636 Burton, T. et al., 2011. *Wind Energy Handbook* 2nd ed., John Wiley & Sons Ltd.

637 van Bussel, G.J.W., 2007. The science of making more torque from wind: Diffuser experiments and
638 theory revisited. *Journal of Physics: Conference Series*, 75(12010).

639 Chapman, J.C. et al., 2013. The Buhl correction factor applied to high induction conditions for tidal
640 stream turbines. *Renewable Energy*, 60, pp.472–480. Available at:
641 <http://dx.doi.org/10.1016/j.renene.2013.05.018>.

642 DNV GL Garrad Hassan, 2012. *Tidal Bladed Theory Manual*,

643 Drela, M., 1989. XFOIL: An analysis and design system for low Reynolds number airfoils. *Low*
644 *Reynolds number aerodynamics*, Volume 54, p.pp 1-12. Available at:
645 http://link.springer.com/chapter/10.1007/978-3-642-84010-4_1.

646 Fleming, C., McIntosh, S.C. & Willden, R.H.J., 2011. *PerAWaT Report: WG3 WP1 D2 Model setup for*
647 *ducted horizontal axis flow turbines*,

648 Fleming, C.F. & Willden, R.H.J., 2016. Analysis of bi-directional ducted tidal turbine performance.
649 *International Journal of Marine Energy*, 16, pp.162–173.

650 Fuglsang, P., Dahl, K. & Antoniou, I., 1999. *Wind tunnel tests of the Risø-A1-18, Risø-A1-21 and Risø-*
651 *A1-24 airfoils*, Roskilde, Denmark.

652 Hansen, 2004. AirfoilPrep excel instructions.

653 Hansen, M.O.L., 2008. *Aerodynamics of wind turbines* second., London, UK: Earthscan.

654 Lawn, C.J., 2003. Optimization of the power output from ducted turbines. *Proceedings of the*
655 *Institution of Mechanical Engineers, Part A: Journal of Power and Energy*, 217(August 2002),
656 pp.107–117.

657 Masters, I. et al., 2011. A robust blade element theory model for tidal stream turbines including tip
658 and hub loss corrections. *Journal of Marine Engineering and Technology*, 10(1), pp.25–35.

659 McIntosh, S.C., Fleming, C. & Willden, R.H.J., 2012. *PerAWaT Report WG3 WP1 D3: Performance and*
660 *wake structure of a model horizontal axis axial flow turbine*,

661 MeyGen, 2016. No Title. *Project Update Spring 2016*. Available at: [http://www.meygen.com/wp-](http://www.meygen.com/wp-content/uploads/Meygen-Newsletter-201602.pdf)
662 [content/uploads/Meygen-Newsletter-201602.pdf](http://www.meygen.com/wp-content/uploads/Meygen-Newsletter-201602.pdf).

663 Moriarty, P.J. & Hansen, a C., 2005. *AeroDyn Theory Manual*, Available at:
664 <http://www.nrel.gov/docs/fy05osti/36881.pdf>.

665 Ning, S.A., 2013. *AirfoilPrep documentation, Technical Report NREL/TP-5000-58817 (release 0.1.0)*,

666 ReNews, 2016. No Title. *Atlantis to decommission SeaGen*. Available at:
667 <http://renews.biz/101295/atlantis-to-decommission-seagen/>.

668 SciPy Community, 2016. SciPy reference guide. *SciPy reference guide v0.18.1*. Available at:
669 <https://docs.scipy.org/doc/scipy-0.18.1/reference/index.html>.

670 Shives, M., 2011. *Hydrodynamic Modeling, Optimization and Performance Assessment for Ducted*
671 *and Non-ducted Tidal Turbines*. Available at:
672 <http://dspace.library.uvic.ca:8080/handle/1828/3801>.

673 Shives, M. & Crawford, C., 2011. Developing an empirical model for ducted tidal turbine
674 performance using numerical simulation results. *Proceedings of the Institution of Mechanical*
675 *Engineers, Part A: Journal of Power and Energy*, 226(1), pp.112–125. Available at:
676 <http://pia.sagepub.com/content/226/1/112.abstract>.

677 Tangler, J.L. & Selig, M.S., 1997. An Evaluation of an Empirical Model for Stall Delay due to Rotation
678 for HAWTS. *Windpower '97*.

679 Turnock, S.R. et al., 2011. Modelling tidal current turbine wakes using a coupled RANS-BEMT
680 approach as a tool for analysing power capture of arrays of turbines. *Ocean Engineering*,
681 38(11–12), pp.1300–1307. Available at: <http://dx.doi.org/10.1016/j.oceaneng.2011.05.018>.

682 UIUC Applied Aerodynamics Group, 2015. UIUC Airfoil Coordinates Database. Available at: [http://m-](http://m-selig.ae.illinois.edu/ads/coord_database.html)
683 [selig.ae.illinois.edu/ads/coord_database.html](http://m-selig.ae.illinois.edu/ads/coord_database.html) [Accessed February 25, 2015].

684 Viterna, L. a. & Janetzke, D.C., 1982. *Theoretical and experimental power from large horizontal-axis*
685 *wind turbines*,

686